*Article*

# Aerodynamic Performance of Vertical-Axis Wind Turbines

**Dmytro Redchyts** [1,*], **Koldo Portal-Porras** [2], **Serhii Tarasov** [1], **Svitlana Moiseienko** [3], **Uliana Tuchyna** [1], **Natalya Starun** [3] and **Unai Fernandez-Gamiz** [2,*]

1  Institute of Transport Systems and Technologies, National Academy of Sciences of Ukraine, 49005 Dnipro, Ukraine; tsv.transmag@gmail.com (S.T.); rododendron40@gmail.com (U.T.)
2  Nuclear Engineering and Fluid Mechanics Department, University of the Basque Country, UPV/EHU, 01006 Vitoria-Gasteiz, Spain; koldo.portal@ehu.eus
3  Section of Higher Mathematics and Mathematical Modeling, Department of General Humanities and Natural Sciences, Kherson National Technical University, 73008 Kherson, Ukraine; 4moiseenko@ukr.net (S.M.); nv_starun@ukr.net (N.S.)
*  Correspondence: redchits_da@ua.fm (D.R.); unai.fernandez@ehu.eus (U.F.-G.)

**Abstract:** The nonstationary separated incompressible flows around Darrieus and Savonius rotors of vertical-axis wind turbines were investigated through computational simulation using the Reynolds averaged Navier–Stokes equations and Spalart–Allmaras turbulence model. The implicit finite-volume algorithm, the basis of which was artificial compressibility method, was chosen to obtain the numerical solution. The series of computational and physical experiments for Darrieus rotors with varied numbers and shapes of blades were performed. The detailed visualization of the flow was presented. The turbulent flows surrounding the Darrieus and Savonius rotors were studied, and as a part of these investigations, the major phases of vortex progress were identified. For this purpose, three series of computer tests on the aerodynamic and power properties of Savonius rotors with two and three buckets were performed, and their results are also presented. The influence of tip-speed ratio, solidity, and Reynolds numbers on the power coefficients of the Darrieus and Savonius rotors was investigated. It has been demonstrated that increasing Reynolds number from $10^4$ to $10^6$ causes a rise in Darrieus rotors power coefficient from 0.15 up to 0.5. The maximum values of power coefficient are moved away from higher values of tip-speed ratio from 2 to 5 as a result of a decrease in Darrieus rotor solidity from 1.0 to 0.33. The greatest power coefficient for a Savonius rotor with two blades is 0.23 and for a Savonius rotor with three blades is 0.19.

**Keywords:** vertical-axis wind turbine; RANS; CFD; aerodynamics

## 1. Introduction

A source of the cheapest electric power produced for commerce and industry in the near future could be wind energy, but the amount of the wind energy generation is still insufficient. Despite the obvious environmental benefits and constant cost reduction, generation of electricity from wind flows in the world is only 5%, which is several times lower than coal- and natural gas-based generation (38%) and (23%), respectively [1].

The biggest share of wind power generation (~85%) is contributed by horizontal-axis wind turbines (HAWT). HAWT has high power coefficients, but requires the use of complex-to-manufacture blades with a variable profile and expensive electromechanical energy conversion devices. The need to reduce the per-unit costs of electricity production has led to the construction of large HAWT with a capacity of several megawatts [2]. Placement of such wind turbines in offshore areas results in their distancing from the final energy consumer. Furthermore, the large size of the HAWT rotors blades (50 m and longer) leads to another problem—reduced service life of the blades due to constant lateral vibrations.

Obviously, aerodynamics is essential to a wind turbines operation. The wind turbine's ultimate efficiency is dependent on the rotor form optimization and aerodynamic properties of the spinning surfaces.

The wind turbine efficiency is defined by the coefficient of performance of a wind power. Results of experimental research showed that high-speed propeller type HAWT and also Darrieus [3] rotors with the fixed and variable pitch blades have high values of performance.

As reviewed by Eriksson et al. [4], vertical-axis wind turbines (VAWT) have a significant disadvantage compared to HAWTs, which is that the power coefficients achievable with this type of turbines are lower, with the power coefficients obtainable with HAWTs to be between 0.4 and 0.5 and the ones obtainable with VAWTs around 0.4. Despite this disadvantage, VAWTs provide numerous advantages compared to HAWTs. Therefore, VAWT could be adopted instead of HAWT. The Darrieus rotor blades have a squared shape and are cheaper to manufacture than the blades of the propeller type HAWT. Since VAWT are not influenced by the wind direction, electromechanical energy conversion devices become simpler, which reduce the operating costs. Because of the VAWT's ease of use, dependability, and capacity to operate in conditions of moderate wind, they can be deployed in remote locations of crucial social significance, see Paraschivoiu [5].

As mentioned previously, VAWTs perform less efficiently in terms of aerodynamics than HAWT. Such a situation is largely caused by a lack of understanding of the VAWT's aerodynamic processes. Another factor is the simplified methodology used to build industrial installations of high-power wind turbines, which ignores the latest achievements of the aerodynamics of the blades in the dynamic stall conditions and is based on empiric hypotheses about the flow pattern around the rotors of VAWTs.

Improving the VAWT designs can be achieved through the use of the Reynolds averaged Navier–Stokes equations (RANS), closed by differential turbulence models, together with the equations of the VAWT rotor dynamic and oscillations. Numerical simulation must be carried out within a wide range of key geometric, mass, and velocity parameters. Despite significant progress in using the methods of computational fluid dynamics (CFD) in solving industrial problems, systematic detailed studies of the flow around the VAWT rotors have actually not been carried out, as stated by Longhuan et al. [6].

Modern trends in design of complex machinery are related with application of complete mathematical models of mechanics of liquid and gas, based on general physical laws (conservation of mass, impulse, energy, rheological relations, dynamics of turbulent whirlwinds). From the mathematical point of view, such models are complicated systems of nonlinear differential equations, which require powerful calculation complexes. For creation of such models, many sections of theoretical and applied mathematics are utilized, namely, analytical and differential geometry, mathematical and, in particular, tensor analysis, mathematical physics, phenomenological principles of modeling, numerical analysis, and computational methodology. Solving of such systems creates a new level of learning when numeral calculations may replace natural experiments, substantially cutting down expenses on tests in wind-channels, which are present in a standard design procedure.

There are four levels of mathematical models of aerodynamics of wind turbines:

I.     Engineering, empirical technique;
II.    Inviscid gas model—The potential and Euler equations;
III.   Viscous gas model with averaging turbulent characteristics (RANS equations);
IV.   Viscous gas models with unsteady turbulent characteristics (DES, LES, DNS approaches).

Nowadays, the first two levels are crucial to wind power design. The specification of the aerodynamic, dynamic, and power properties of wind turbine rotors is commonly conducted using methods that are based on experimental data, such as in Brochier et al. [7] and Hu et al. [8], impulse and vortex theories, as in Strickland [9], and the computational solution of the potential and Euler equations. These methods rely among others on quasi-steady flow and ignorance viscous–inviscid interaction assumptions. The impact of dynamic stall on the computation of nonstationary stream around rotors of wind turbine is the main challenge, see Biadgo et al. [10]. Until now, simplified models have provided aerodynamic estimates with insufficient accuracy, particularly in the situation of dynamic stall.

Passing to the third level of simulation of aerodynamic flows, it is possible to state that calculations on the basis of RANS equations are becoming widely used in industrial practice. Sun et al. [11] studied operating variations of a Darrieus VAWT by means of RANS equations, and Gonzalez Madina et al. [12] studied that of a Savonius [13] VAWT.

The fourth level is research in computational fluid dynamics. It is rather expensive even for industrialized countries, and its introduction in the industry is predicted for second half of the 21st century. Nevertheless, some authors have used the approaches mentioned above for VAWT analysis. For example, Abkar and Dabiri [14] used LES for flow characteristics prediction of the wake behind a VAWT, and Nguyen et al. [15] used DNS methods. Sheidani et al. [16] used both LES and RANS models for predicting the wake behind a VAWT, showing that RANS methods provide accurate predictions of the wake region length and width, and therefore, they are suitable for obtaining an overall view of the wake region. However, LES is able to predict more flow structures than RANS, especially in the internal wake region.

In recent works, Crooks et al. [17] conducted a computational design analysis study of a counter-rotating Darrieus turbine system, Karimian and Abdolahifar [18] proposed a new Darrieus design to benefit from straight-blade and helical-blade VAWTs, and Dadamoussa et al. [19] added Vortex Generators on the blades of a Darrieus VAWT, improving its performance. Al-Gburi et al. [20] compared the influence of several parameters on the performance of a Savonius rotor, and Altan and Gultekin [21] proposed additional design processes for Savonius rotor performance enhancement.

The aim of this paper is to study the structure and determine the main energy parameters of the unsteady flow around vertical-axis wind turbines with Darrieus and Savonius rotors based on the developed specialized CFD code.

The novelty and main contributions of this paper:

1. The regularities of the development of the unsteady flow around Darrieus and Savonius rotors with different number of blades have been revealed.
2. Qualitative comparisons of the flow pattern around a two- and three-blade Darrieus rotor with experimental data were carried out.
3. The dependences of the power coefficient of the VAWT rotors on the Reynolds number, tip-speed ratio, and solidity are determined.
4. The influence of the Reynolds number on the dynamic stall from the blades and the Darrieus rotor power coefficient is determined.
5. The influence of the solidity and the tip-speed ratio on the power characteristics of the Darrieus rotor is determined.
6. The influence of the blades number and Reynolds number on the power characteristics of the Savonius rotor is determined.

The following manuscript is divided as follows: Section 2 explains the tested cases and numerical methodology, Section 3 details the numerical algorithm used for the simulations and describes the developed CFD code, Section 4 shows the obtained results, and Section 5 summarizes the main findings of this study.

## 2. Methodology

The orthogonal Darrieus and Savonius rotors are investigated in this study (Figure 1).

The normal blades are substantially longer than the chord, which enables one to ignore end effects on the blades and to use the plane-parallel structure of flow hypothesis. As a result, the study assumes a two-dimensional statement in a plane that is perpendicular to the rotor's rotational axis. The rotors of Darrieus and Savonius are considered to be completely rigid. Incompressible RANS equations closed by the Spalart–Allmaras (SA) eddy viscosity turbulence model are used to describe the aerodynamic processes of wind turbines. These equations are straightforward, trustworthy, and suitable for a variety of external flows. For example, Shukla and Kaviti [22] demonstrated the reliability of this model for a VAWT with different airfoils.
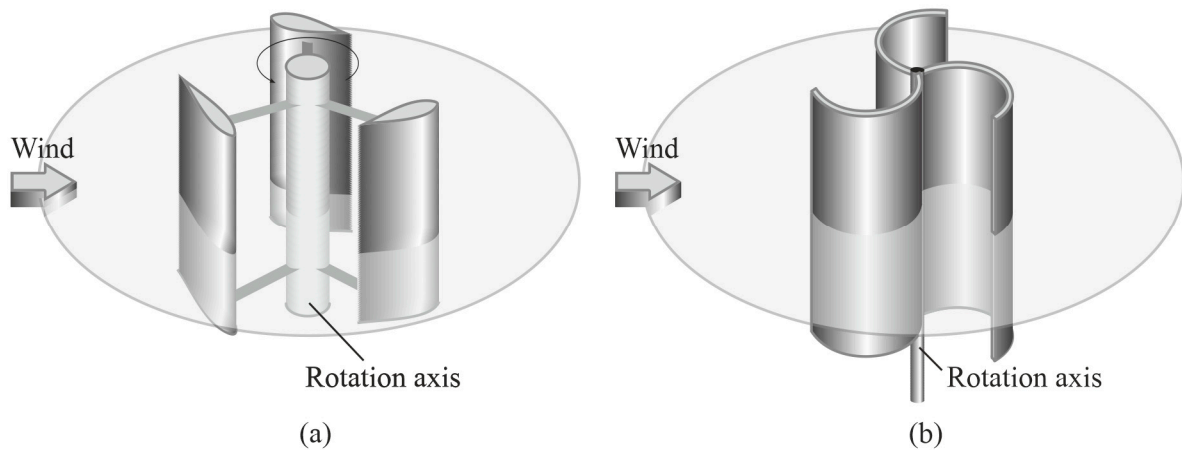
**Figure 1.** Computational schemes of Darrieus (**a**) and Savonius (**b**) rotors.

### 2.1. Mathematical Model

The low-speed air movement at low Mach numbers (M < 0.3) is examined in this work. Since the effects of air compressibility may be ignored in this situation, the simulation of the turbulent flow under investigation has been conducted using the incompressible RANS equations for a viscous flow (in Cartesian tensor form) [23]

$$\frac{\partial u_j}{\partial x_j} = 0 \tag{1}$$

$$\frac{\partial u_i}{\partial t} + \frac{\partial (u_j u_i)}{\partial x_j} = -\frac{1}{\rho}\frac{\partial p}{\partial x_i} + \frac{\partial}{\partial x_j}\left[(v + v_t)\left(\frac{\partial u_i}{\partial x_j} + \frac{\partial u_j}{\partial x_i}\right)\right] \tag{2}$$

where $M = u/u_\infty$ is Mach number; $u_\infty$ is the free stream velocity, which used the definition of the Reynolds number too; $u_i$ are the Cartesian components of the velocity vector; $x_i$, $i = 1, 2$ are the Cartesian coordinates, m; $t$ is time, s; $\rho$ is density, kg/m$^3$; m/s; $p$ is pressure, Pa; $v$ and $v_t$ are the kinematic coefficients of molecular and turbulent viscosity, m$^2$/s, correspondingly.

### 2.2. Turbulence Model

The RANS equations are closed by using the differential single-parametric SA turbulence model [18]. The goal of the conventional SA model is to calculate the turbulent viscosity's dimensional kinematic coefficient

$$v_t = \tilde{v}_t \cdot f_{v1}, \quad f_{v1} = \chi^3 / \left(\chi^3 + c_{v1}^3\right) \tag{3}$$

where $f_{v1}$ is a damping function of kinematic viscosities $\chi$, $\tilde{v}_t$ is the working variable, m$^2$/s, $c_{v1} = 7.1$. In the SA model the equation to determine $\tilde{v}_t$ takes the form [24]

$$\frac{D\tilde{v}_t}{Dt} = c_{b1}\tilde{S}\tilde{v}_t + \frac{1}{\sigma}\frac{\partial}{\partial x_i}\left[(v + \tilde{v}_t)\frac{\partial \tilde{v}_t}{\partial x_i}\right] + \frac{c_{b2}}{\sigma}\frac{\partial \tilde{v}_t}{\partial x_i}\frac{\partial \tilde{v}_t}{\partial x_i} - f_w\left(\frac{c_{b1}}{k^2} + \frac{1+c_{b2}}{\sigma}\right)\left(\frac{\tilde{v}_t}{d}\right)^2 \tag{4}$$

The source term for turbulence generation is the first term on the equation's right-hand side (4)

$$\tilde{S} \equiv f_{v3}W + \frac{\tilde{v}_t}{k^2 d^2}f_{v2}, \ W = \sqrt{2W_{ij}W_{ij}} \tag{5}$$

where $W_{ij}$ is the vorticity tensor, 1/s, $k = 0.41$.

The function $f_{v2}$ is determined from the relation

$$f_{v2} = 1 - \frac{\chi}{1 + \chi f_{v1}} \tag{6}$$

The turbulence dissipation is caused by the second and third terms in the right-hand section of Equation (4). The fourth one has a function and is the dissipation of turbulence nearby a solid wall.

$$f_w = g \left[ \frac{1 + c_{w3}^6}{g^6 + c_{w3}^6} \right]^{1/6}, \ g = r + c_{w2}(r^6 - r), \ r = \frac{\widetilde{v}_t}{\widetilde{S}k^2 d^2}, \tag{7}$$

where $d$ is distance from the nearest wall, m. The values for other non-dimensional constants are [24]

$$c_{b1} = 0.1355, \ c_{v2} = 5.0, \ \sigma = 2/3, \ c_{b2} = 0.622, \ c_{w1} = \frac{c_{b1}}{k^2} + \frac{(1 + c_{b2})}{\sigma}, \ c_{w2} = 0.3, \ c_{w3} = 2.$$

The traditional terms of SA model, containing $f_{t1}, f_{t2}$ and responsible for near-wall treatment for adequate reproduction of laminar–turbulent transition behavior, are not presented in the applied model version due to the fact that the laminar flow zones are negligible in comparison with the prevailing turbulent flow mode.

### 2.3. Boundary Conditions

No-slip boundary conditions are set on the body surfaces. By defining a zero-pressure gradient normal to the wall, the pressure is obtained. To determine the dependent variables at the outer boundary of the computational domain, non-reflecting boundary conditions based on the method of characteristics [25,26] are used.

## 3. Numerical Setup

### 3.1. Numerical Algorithm

The coordinate system for the governing equations was arbitrarily curvilinear. To calculate nonstationary flows, the artificial compressibility approach was used to agree to the pressure and velocity fields. The basic equations were converted into discrete forms using the structured grids. The multi-block computation methods were applied in places that were not just directly connected (Figure 2). Each block in an intersecting grid and may have a variable size. This strategy made it possible to provide a standardized system for estimating viscous fluid flows around objects with complex geometries.

The calculation grids were built by the method of many surfaces [27]. The outer boundary is a circle with a radius of 40. All grids (domains) were rigidly connected to each other and rotated synchronously with the rotor blades relative to the center.

The dimension of the grids (the number of nodes in each direction) is not explicitly related to each other. The transfer of information from one computational domain to another is performed through their mutual overlap by means of interpolation relations linking dependent variables in the nodes of neighboring grids.

The computational grid around the Savonius rotor was a single-block O-type mesh with a total number of nodes of about one million ($1050 \times 980$) (Figure 2a). A multi-block mesh with a total number of nodes of about 600 thousand was used around the Darrieus rotor (Figure 2b). A separate O-type mesh was built around each element of the Darrieus rotor, which intersected with neighboring meshes by at least two nodes. The first grid spacing near the surface was $10^{-6}$, which ensured the fulfillment of the condition $y^+ < 1$ for all computational cases.
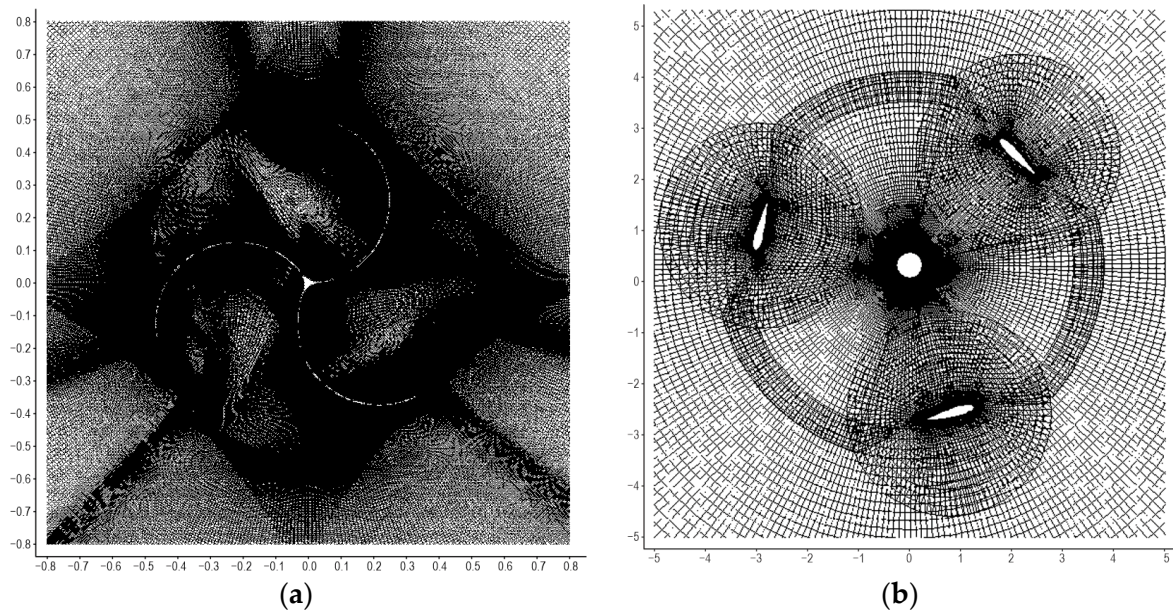
**Figure 2.** Calculation grids: (**a**) structured single-block around the Savonius rotor; (**b**) structured multi-block around the Darrieus rotor.

In order to preserve the third order of approximation of convective terms in the transport equations, each node should have at least two neighboring nodes on each side when using a single-block grid. The order of approximation of convective terms can be decreased to a second one only for nodes located near the body surface or outer boundary of the computational domain. Based on these considerations, the minimum overlapping area of the computational grids should contain at least four nodes. Bicubic interpolation is used to determine the dependent variables at the inner boundaries of the computational blocks.

Using the finite volume method, the initial equations were numerically integrated. For convective terms, the third-order upwind Rogers–Kwak technique [28] was utilized. Convective terms in the turbulence model were approximated using the TVD scheme and a third-order ISNAS (Interpolation Scheme which is Non-oscillatory for Advected Scalars) flow limiter. A second-order central difference technique was used to approximate the derivatives in terms of viscosity. The algorithm for solving the equations is based on a three-level second-order time-accurate implicit system with sub-iterations in pseudo-time. The generalized minimal residual (GMRES) approach with ILU(k) pre-conditioning was employed to solve the resultant block-matrix system of linear algebraic equations.

### 3.2. Developed CFD Code

The author's team used the specific CFD program created by Redchyts [29] in the context of this work. This software makes it possible to obtain the required level of compromise between the required processing resources and the quality of the results. The established computational methodology's foundational framework offers a comprehensive CFD approach based on the Navier–Stokes equations, including the RANS technique, a number of differential turbulence models, and a multi-block method for the flows in the multiple intersected domains.

On the one hand, a complete computational fluid dynamics approach based on the Navier–Stokes equations was implemented. On the other hand, the analysis of the physics of flow around orthogonal Darius and Savonius rotors allowed us to reduce the problem statement to a two-dimensional plane (Figure 1). This made it possible to reduce computational costs without compromising the reliability of the numerical experiment and to bring the calculation of unsteady flow to 50–100 h on a standard personal computer.

The developed specialized CFD package is written in Fortran 90 and allows solving two-dimensional unsteady laminar and turbulent flows of liquid and gas in arbitrary

geometry. The package generates meshes using the multi-surface method [27]. It is also possible to import grids from external mesh generators.

The development of CFD tools made it possible to handle problems in dynamics and aerodynamics as well as electrochemistry, multiphase fluids, combustion, and plasma kinetics. The fresh technical concepts developed, and new knowledge about the physics of flow separation and how to control it, enable to replicate the actual CFD code structure to many flow types over a wide speed range.

The pre-processor, the computing core, and the postprocessor are the three standard primary components of the generated specialized CFD code, just as in other comparable commercial and opensource software. The development of the basic geometry, the production of discrete space, and the movement of specific computational grid blocks are all intended uses for the pre-processor. In the computing core, the equations of dynamics of a viscous incompressible medium and a solid are integrated, the turbulence parameters are calculated, the boundary conditions are met, and the integral characteristics of the VAWT rotor are determined as functions in time. The post-processor is used to process integral flow parameters over time (such as the calculation of aerodynamic characteristics), prepare data for external visualizers, and perform built-in visualization of the findings (scalar and vector values). Benefits of house-developed package:

-       the main task of the specialized package is to simulate the flow field numerically with maximum physical veracity;
-       specialization of the package and the efficiency of solving this class of problems;
-       no need to buy or rent expensive commercial packages.

This package has been developed since 2005 and was initially focused on solving the problems of unsteady flow around bodies with moving boundaries. The pre- and post-processing tools, including the solver, are purposefully designed for maximum convenience and efficiency while being inexpensive for priority application to these flows. In addition, the presence of a package of our own design allows us to develop it in the future in any desired direction, depending on the tasks that will be relevant to the solution. This approach, for all its cost in terms of writing and debugging software code, makes it independent of the general trends in the CFD software market.

Modern verification methods and careful testing of the developed programs are absolutely necessary to verify the obtained numerical results and the reliability of the CFD methods. To verify the developed numerical methods, the test calculations of a series of problems such as laminar and turbulent flow around a stationary and rotating cylinder [29], subcritical and supercritical flow around stable and oscillating airfoils NACA 4412 and NACA 0015, aerodynamics of turbulent flow around a 30P30N three-element airfoil in a crash and landing configuration [30], and turbulent flow around a cargo truck-trailer [31] have been performed.

## 4. Results and Discussion

### 4.1. Darrieus Rotor

The results of numerical simulation of the flow around a rotating single blade of the Darrieus rotor are presented (Figure 3). The initial data for the numerical simulation were acquired from an experimental work [32] for the case of flow around a single Darrieus rotor blade in the presence of dynamic stall. At the tip-speed ratio $\lambda = 2.5$ and Reynolds number Re = 67,000, dynamic separation of the flow from the blade of the Darrieus rotor is observed over most of the trajectory. It is characterized by the flow separation from the leading edge of the blade and the formation of large vortex structures that are carried along the chord of the blade. The absolute velocity change along the circumference of the rotation blade leads to a larger area of dynamic stall in that part of the trajectory where the blade and flow velocities are in the same direction. In this zone, the incident stream carries the vortices in the direction of the blade movement. On the second half of the trajectory, the flow carries the vortices in the direction opposite to the movement of the blade. In this case, the duration of the dynamic stall is less than in the previous one.
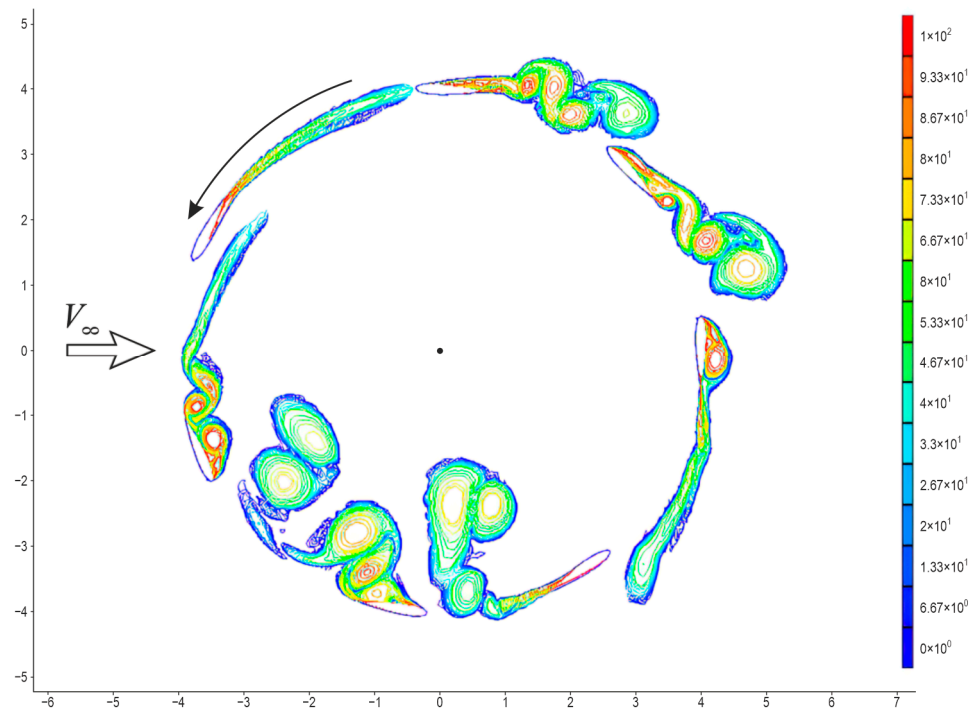
**Figure 3.** Reconstruction of the flow field around one-blade Darrieus rotor.

The value of the angle $\theta = 0°$ corresponds to the rotor position when the leading edge of the blade is directed towards the flow. On the windward part of the blade trajectory, the blade angle increases, the pressure coefficient on the inner surface of the blade decreases. This leads to an increase in the absolute values of the lift coefficient, which makes the main contribution to the torque (Figure 4).
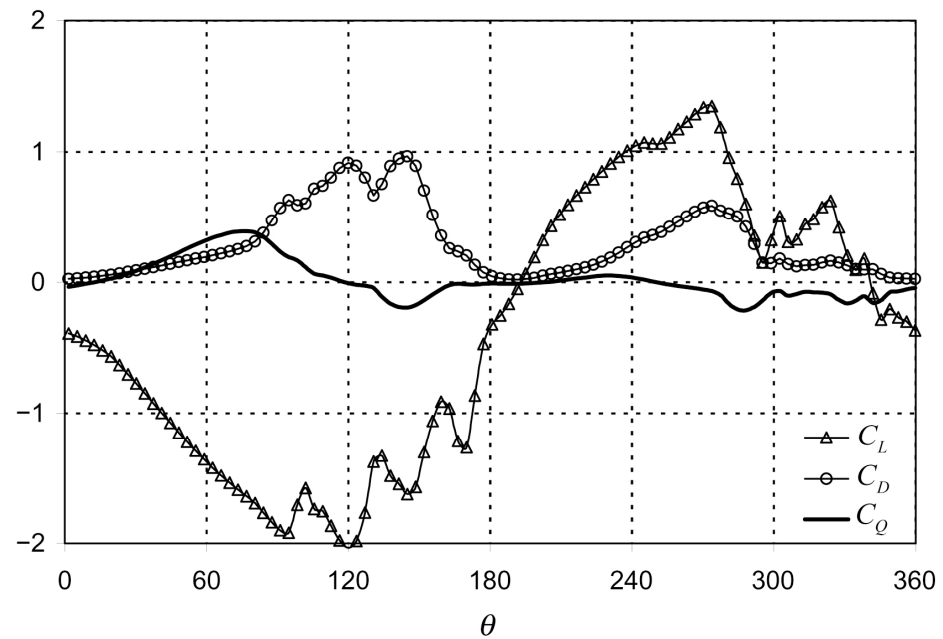


**Figure 4.** Change of lift $C_L$, drag $C_D$, and torque $C_Q$ coefficients of the blade depending on the rotor angular position $\theta$.

The boundary layer separated near the trailing edge of the blade, and the position of the separation point is shifted towards the leading edge of the blade. This leads to the separation of the vortex from the leading edge of the blade and subsequent movement along

the chord towards the trailing edge of the blade. A drop in the lift and drag coefficients is observed (Figure 4). On the leeward part of the blade trajectory, the streamline pattern and aerodynamic coefficient behavior is somewhat different from the windward part.

The dependence of non-averaged coefficients of lift force $C_L$, drag force $C_D$, and torque $C_Q$ on the angular position of the rotor are shown in Figure 4. At the tip-speed ratio $\lambda = 2.5$, the maximum of torque coefficient $C_Q = 0.4$ is observed at rotor angle $\theta = 80°$. After reaching the maximum of torque coefficient, it drops to values of $C_Q = -0.2$, which corresponds to the rotor angle $\theta = 145°$. In this range of angular positions, the Darrieus rotor is subject to dynamic stall. Subsequently, when flow attachment $\theta = 190°$ occurs, the value of torque coefficient has a positive value up to angle $\theta = 250°$. Further increasing of angle leads to dynamic stall of flow from the outside surface of the blade, and torque coefficient becomes negative (Figure 4).

The values of the torque and power coefficients of a single blade of the Darrieus rotor averaged over one revolution have the following values $\overline{C}_Q = 0.11$ and $\overline{C}_P = 0.044$, respectively.

Only symmetric airfoils from NACA00XX family are considered in the majority of experimental and theoretical studies [7–9], analyzing the flow structures of the Darrieus rotor and its power coefficients. The overall structure solidity may vary if one or several blades are added. In present paper, the VAWT with NACA 0018 airfoil blades [10,11] at zero angle of attack is studied.

For a two-blade Darrieus rotor, flow visualization and reconstruction have been carried out using physical [7] and computational experiments (Figure 5). Only the vortices with the highest intensity are shown for better clarity. At various points along the trajectory of the blade, the stages of vortex creation, development, and stall are presented. The flow around the blade has an associated character at the start of a leeward side of a trajectory and before rotor angle of 234 degrees. At the rotor angle (240°) specified, a separated flow is formed. Vortices split from the blade leading edge and start moving along a surface when there is dynamic stall on the inner surface [32–34].

The calculations were carried out in two stages. In the first stage, an undisturbed flow was set in the computational domain. In the second stage, the flow structure was studied at a fixed tip-speed ratio, and the main parameters of the unsteady flow of the Darrieus rotor were determined.

The three-blade Darrieus rotor's flow pattern is presented by the physical investigation [35] (Figure 6a). Numerical simulation was carried out with tip-speed ratio of $\lambda = 3$ (Figure 6b). Dynamic separation of the flow from the blade of the Darrieus rotor is observed on most of the trajectory. A series of large, counter-rotating vortices make up the instantaneous flow structure. The main reason for the dominance of dynamic vortex shedding over most of the blade trajectory is the low Reynolds number Re = 1470, which corresponds to the initial stage of the transition from laminar to turbulent flow. Different areas of the blade trajectory exhibit asymmetries. The majority of shed vortices are more intense than the vortices traveling with the flow. This is as a result of the relative flow velocity being higher at this point in the blade trajectory than it is at the opposite point. A cluster of vortices that were created by the first blade is present in the front portion of the Darrieus rotor. There is an accumulation of vortices created by earlier blades downstream.
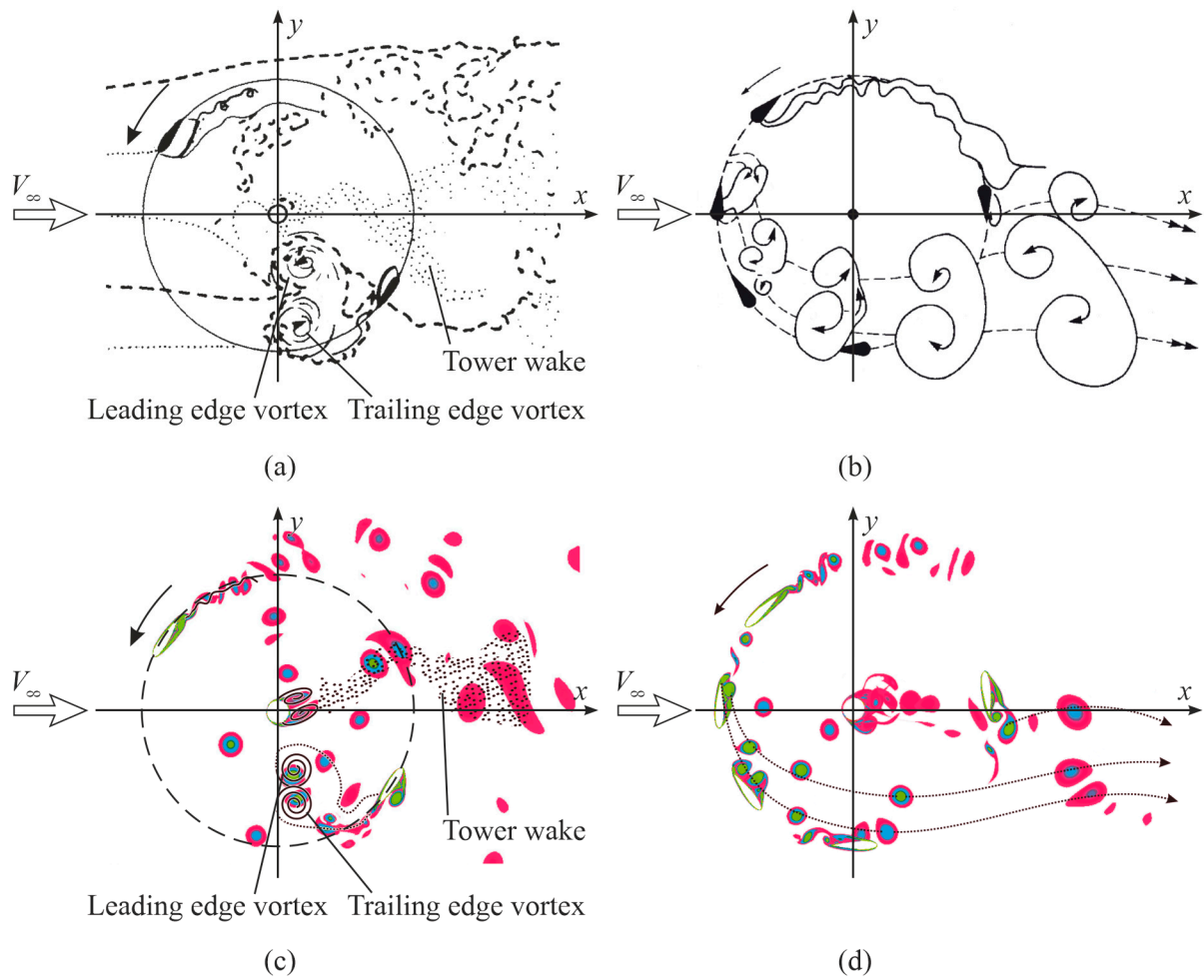
**Figure 5.** Visualization (**a**,**c**) and reconstruction (**b**,**d**) of the flow around Darrieus rotor of two blades based on experimental [7] (**a**,**b**) and computational (**c**,**d**) results.
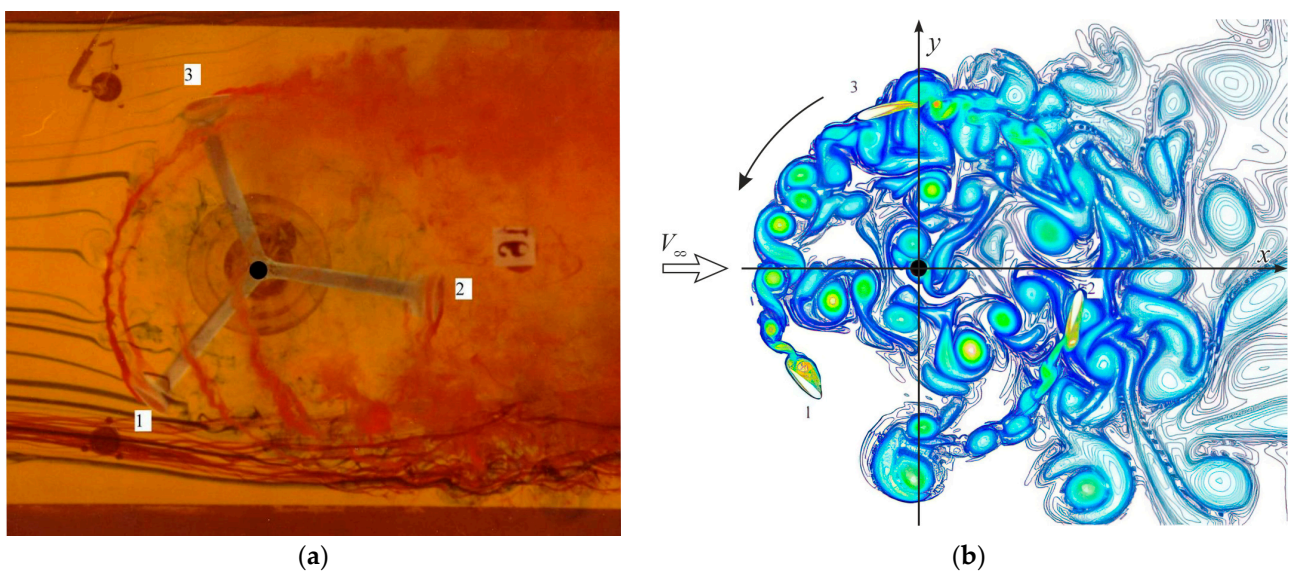


**Figure 6.** Visualization of the flow field during operation of the three-blade Darrieus rotor for the speed coefficient λ = 3 based on physical (**a**) and computational (**b**) experiments [35].

For the parameters under consideration, the stream pattern is distinguished by fundamentally unstable effects, such as stalling, the creation of intricate vortex ensembles, and interactions between vortices of various intensities, sizes, and speeds and the rotor surface. The impact of tip-speed ratio, solidity, and Reynolds numbers on the power coefficients of the Darrieus rotors was investigated (Figure 7). The main parameters of computational experiments:

- Blade airfoil—NACA 0018;
- Tip-speed ratio—$\lambda = 0 \ldots 7$;
- Reynolds number on the rotor diameter—$\mathrm{Re}_D = 10^4$, $\mathrm{Re}_D = 10^5$, $\mathrm{Re}_D = 10^6$;
- Solidity—$\sigma = 0.33$, $\sigma = 0.67$, $\sigma = 1$.
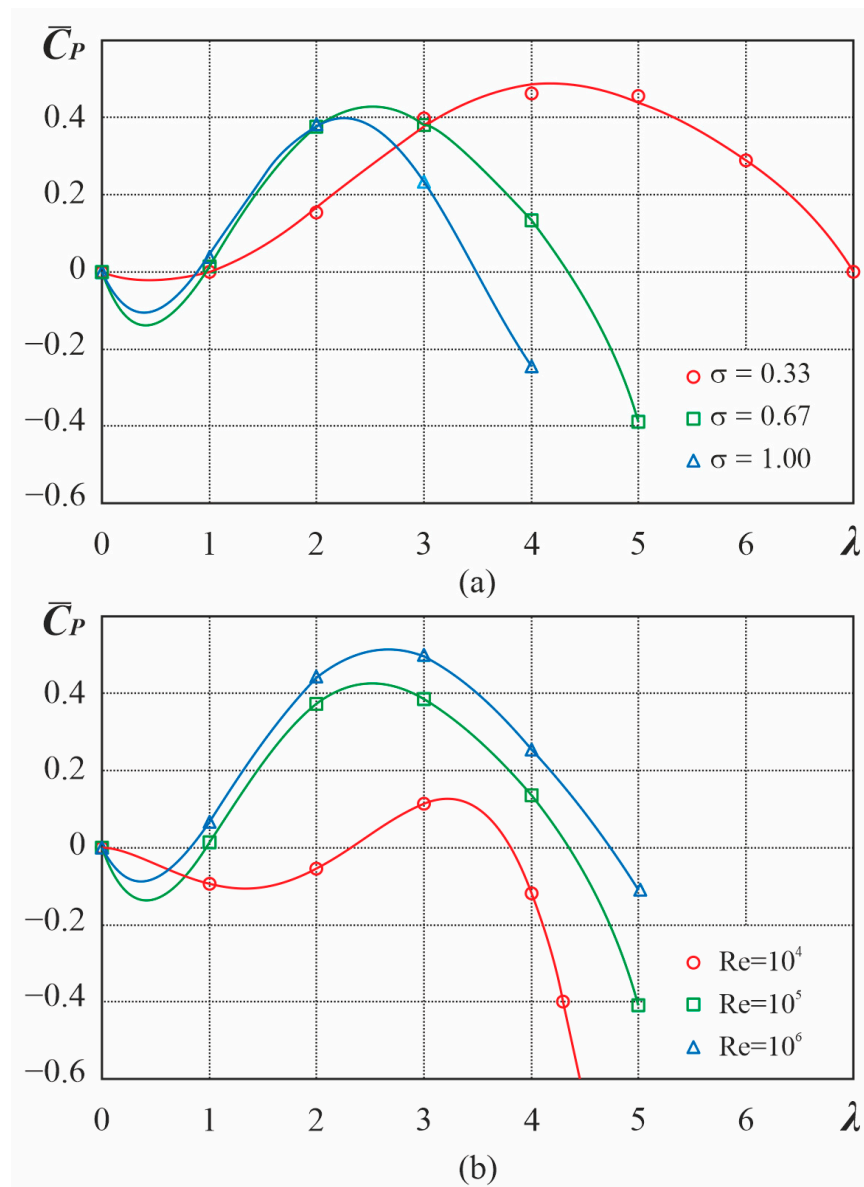


**Figure 7.** Influence of solidity $\sigma$ (**a**) and Reynolds numbers (Re) (**b**) on Darrieus rotor power coefficient $\overline{C}_P$.

It has been demonstrated that increasing Reynolds number from $10^4$ to $10^6$ causes a rise in power coefficient from 0.15 up to 0.5. The maximum values of power coefficient are moved away from higher values of tip-speed ratio from 2 to 5 as a result of a decrease in Darrieus rotor solidity from 1.0 to 0.33 [32,33].

The overestimated values of the Darrieus rotor power factor by 10–20% are the result of a somewhat idealized mathematical model. The developed model does not take into account the three-dimensional effects, end effects, large-scale turbulence, the effects of the laminar–turbulent transition, and rotor power losses due to the electro-mechanical part of the rotor. Accounting for these effects will be the focus of our further research.

### 4.2. Savonius Rotor

This paper presents the findings from three sets of simulations on the aerodynamic and power properties of Savonius rotors with two and three blades. In [36], an experimental study of a two- and three-bladed Savonius rotor in a low-speed wind tunnel was carried out in order to determine the aerodynamic and energy characteristics. The undisturbed flow velocity was $U_\infty = 7$ m/s and $U_\infty = 14$ m/s, which corresponds to the Reynolds numbers calculated from the rotor diameter Re $= 4.32 \times 10^5$ and Re $= 8.64 \times 10^5$, respectively.

*The geometry of a two-blade Savonius rotor.* The rotor blades have semicircles with radius $r = 0.25$ m in their cross section [36]. The rotation radius was measured from the rotation axis to the outer edge of the blades. The computational grid contained $800 \times 600$ nodes.

*The geometry of a three-blade Savonius rotor.* The arc of the blades in the Savonius three-bladed rotor was reduced by 20 at the outer edge [36]. The calculated grid contained $1050 \times 980 \approx 10^6$ nodes. A detailed grid is necessary to adequately represent the complex geometry of the Savonius rotor and to qualitatively account for the processes in the turbulent boundary layer.

The duration of one computational experiment on a personal computer was about 100 h.

A stable Savonius rotor that was fixed at different angles of attack was the subject of the first set of computational experiments. The time-averaged torque coefficients for the two-blade Savonius rotor are positive for most angular positions, but they are negative for angles between 55 and 80 degrees. Torque coefficients for three-blade designs are always positive.

The Savonius rotor's fixed tip-speed ratio was the subject of the second set of simulations (Figure 8). The maximum torque coefficient for Savonius rotors with two blades is 0.4, while for those with three blades, it is 0.35. (Figure 9). They match a tip-speed ratio of 0.40. The greatest power coefficient for a Savonius rotor with two blades is 0.23 and for a Savonius rotor with three blades is 0.19. The obtained results and the experimental data are adequately matched [32,33].
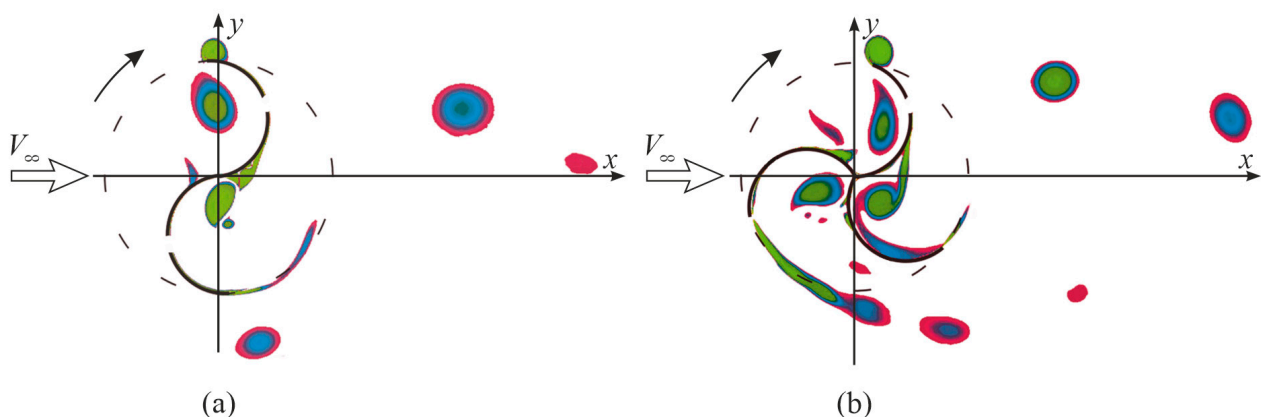


(a)         (b)

**Figure 8.** Flow fields around the rotating Savonius rotor with two (**a**) and three (**b**) blades, respectively, based on computer experiments.

The solution to the joined problem of the aerodynamics and dynamics of the three-blade Savonius rotor is represented by the third series of computational experiments. Three phases of calculations were performed. The first stage's goal was to identify a periodic stream with a Karman vortex street-like shape (Figure 10a). The coupled equations governing the rotation and aerodynamics of Savonius rotors were solved in the second and third stages (Figure 10a,b). When the rotor is unlocked, the incoming wind flow causes it to start rotating, intensifying the vortex formation. Incoming stream speed, distinctive size, and VAWT rotation velocity all affect how often vortices were detached. The Savonius rotor was subjected to load torque in the third stage (Figure 10c), which stabilized the rotor's angular speed and caused close to cyclic fluctuations in the drag, lift, and torque coefficients [32,33].
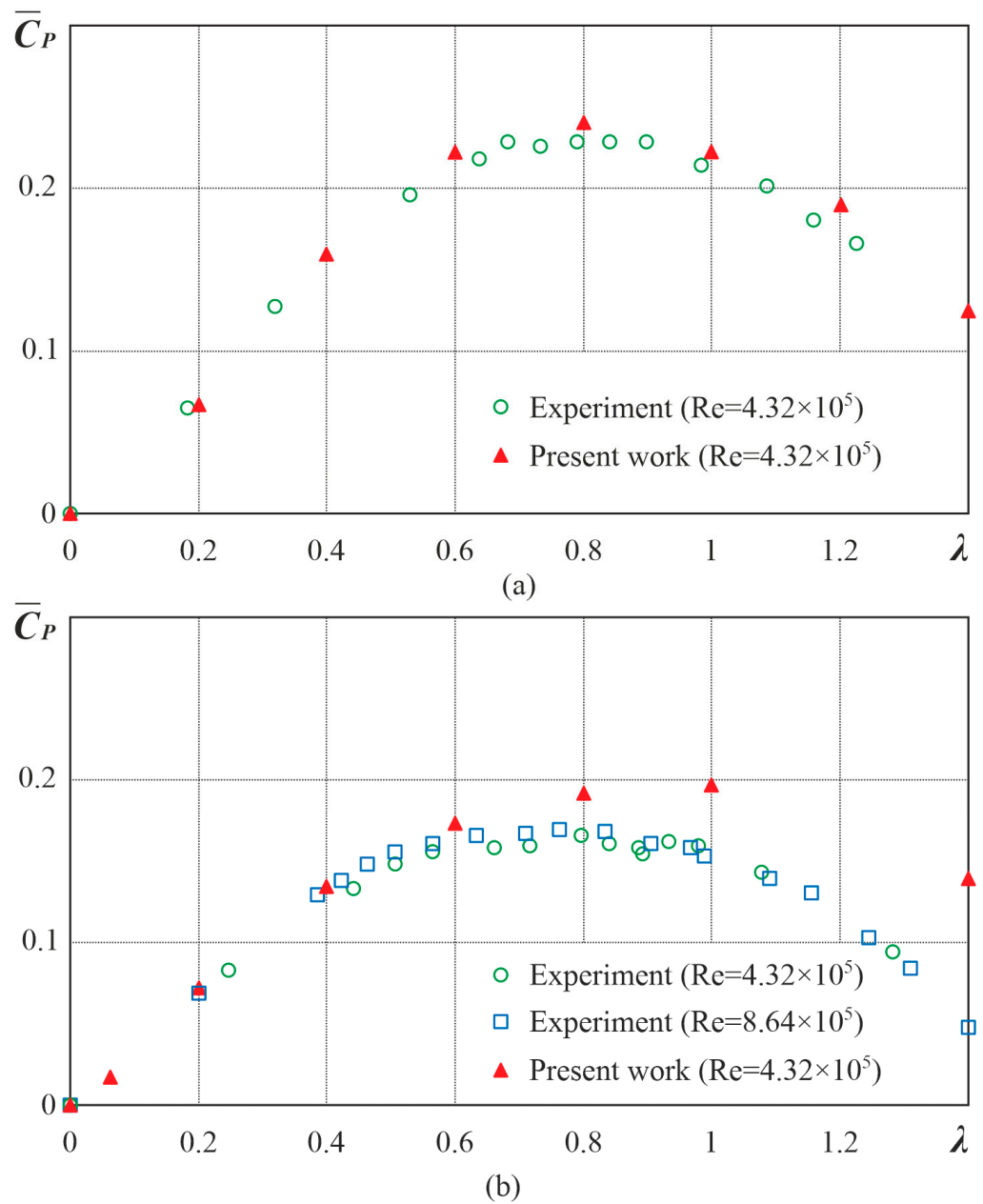


**Figure 9.** Two- (**a**) and three-blade (**b**) Savonius rotor power characteristics based on physical [36] and computational experiments.
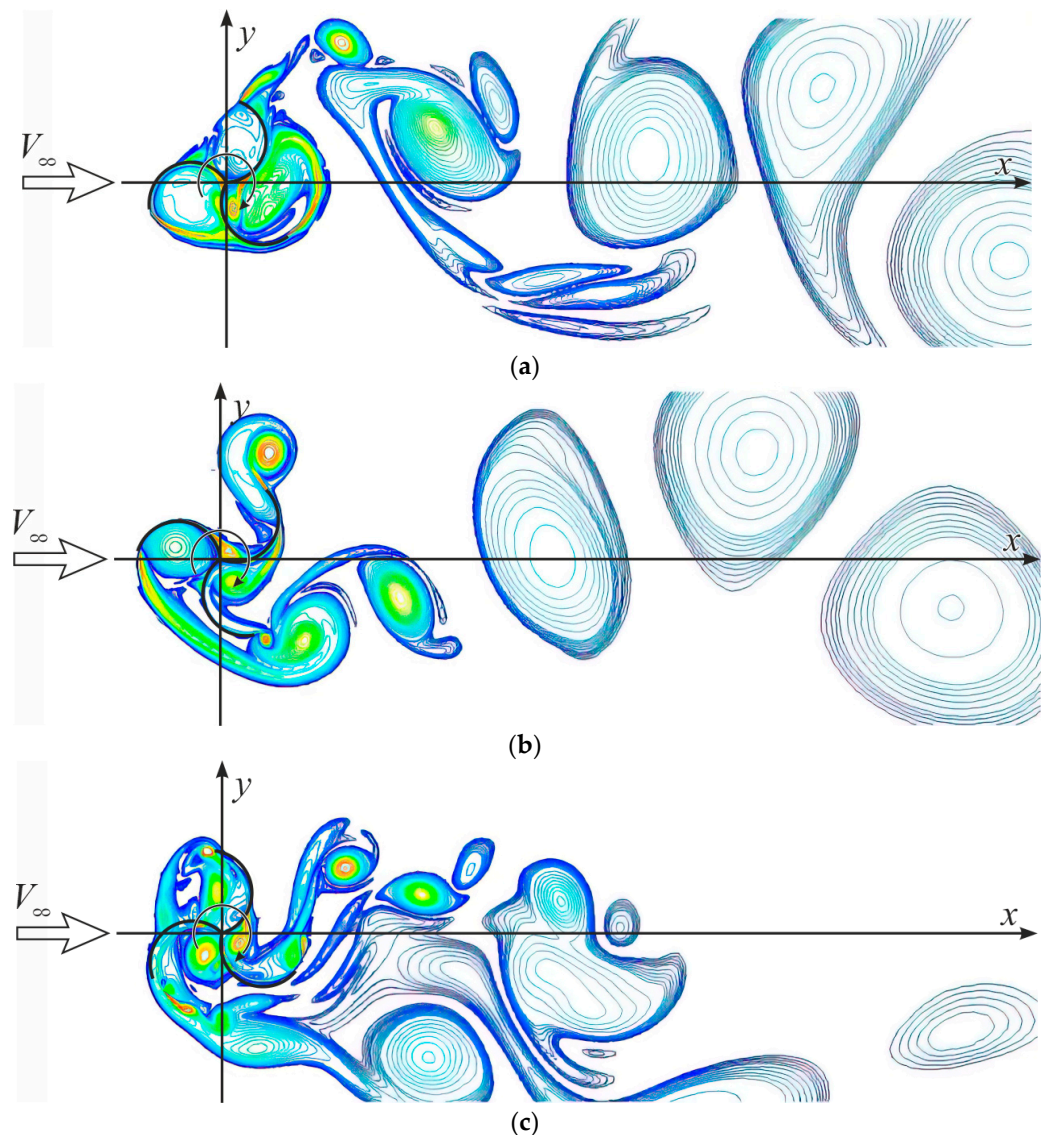
**Figure 10.** Flow fields around the non-rotating (**a**) and rotating (**b**,**c**) three-blade Savonius rotor.

## 5. Conclusions

Using the developed specialized CFD code based on the Reynolds averaged Navier–Stokes equations with turbulence model, new solutions for the unsteady flow around the rotors of the VAWT with Darrieus and Savonius rotors are performed. The finite volume approach was used to numerically integrate the set of governing equations. Convective terms were approximated to third-order accuracy using the Rogers–Kwak counter-flow scheme. The turbulence model's convective component was simulated using a TVD scheme with a third-order ISNAS flow limiter. Two different varieties of Darrieus and Savonius rotors, with different numbers of blades and geometries, have their properties estimated and researched. The investigation of the growth of turbulent unstable incompressible flows around the VAWT Darrieus and Savonius rotors was conducted. Qualitative comparisons of the flow pattern around a two- and three-blade Darrieus rotor with experimental data have been carried out. The regularities of unsteady flow development around Darrieus and Savonius rotors with different number of blades have been revealed. The dependences of the power coefficient of the VAWT rotors on the Reynolds number, tip-speed ratio, and solidity are determined. It is shown that the dynamic stall from the blades of the Darrieus rotor at low Reynolds numbers is observed on most of the blade trajectory. It is established that an increase of the Reynolds number (from $10^4$ to $10^6$) leads to an increase

of the Darrieus rotor power coefficient (from 0.1 to 0.5). It was found that a decrease of the Darrieus rotor solidity (from 1 to 0.33), the power coefficient becomes less sensitive to changes of the tip-speed ratio. It is shown that the optimal values of the tip-speed ratio (from 2 to 5) significantly depend on the Reynolds number and the Darrieus rotor solidity. On the basis of computational and natural experiments, it is shown that the maximum power coefficient of a two-blade Savonius rotor (0.23) is higher than that of a three-blade rotor (0.19).

The developed specialized CFD code can be used in the design and development of new wind turbines and selection of a rational rotor shape and wind turbine operating modes. The obtained parametric dependencies can be used to improve existing engineering and semi-empirical methods.

The direction of further research will be the application of the $\gamma$-$Re\theta$ transition model for this class of flows together with the SA turbulence model and the comparison of the obtained results with experimental and computational data of other authors. It is also planned to develop a specialized package for solving three-dimensional incompressible Navier–Stokes equations for the calculation of arbitrarily shaped bodies.

## References

1. Electricity Information. 2019. Available online: https://www.iea.org (accessed on 5 June 2023).
2. Global Wind Report (GWEC). 2019. Available online: https://gwec.net/global-wind-report (accessed on 5 June 2023).
3. Darrieus, G.J.M. Turbine Having Its Rotating Shaft Traverse to the Flow of the Current. U.S. Patent 1,835,018, 8 December 1931.
4. Eriksson, S.; Bernhoff, H.; Leijon, M. Evaluation of different turbine concepts for wind power. *Renew. Sustain. Energy Rev.* **2008**, *12*, 1419–1434. [CrossRef]
5. Paraschivoiu, I. *Wind Turbine Design with Emphasis on Darrieus Concept*; Polytechnic International Press: Burlington, ON, Canada, 2002.
6. Longhuan, D.; Grant, I.; Robert, D. A review of H-Darrieus wind turbine aerodynamic research. *J. Mech. Eng. Sci.* **2019**, *233*, 7590–7616.
7. Brochier, G.; Fraunie, P.; Beguier, C.; Paraschivoiu, I. Water channel experiments of dynamic stall on Darrieus wind turbine blades. *J. Propuls.* **1986**, *5*, 445–449. [CrossRef]
8. Hu, Y.; Wang, T.; Jin, H.; Cao, X.; Zhang, C. Experimental study on aerodynamic characteristics of vertical-axis wind turbine. *Int. J. Smart Grid Clean Energy* **2017**, *2*, 104–113. [CrossRef]
9. Strickland, J.H.; Webster, B.T.; Nguyen, T. Vortex model of the Darrieus turbine: An analytical and experimental study. *NASA STI/Recon Tech. Rep. N* **1980**, *80*, 25887. [CrossRef]
10. Biadgo, A.; Simonovic, A.; Komarov, D.; Stupar, S. Numerical and Analytical Investigation of Vertical Axis Wind Turbine. *FME Trans.* **2013**, *1*, 132–150.
11. Sun, X.; Wang, Y.; An, Q.; Cao, Y.; Wu, G.; Huang, D. Aerodynamic performance and characteristic of vortex structures for Darrieus wind turbine. II. The relationship between vortex structure and aerodynamic performance. *J. Renew. Sustain. Energy* **2014**, *6*, 043135. [CrossRef]

12. Madina, F.G.; Gutiérrez, A.; Galione, P. Computational fluid dynamics study of Savonius rotors using OpenFOAM. *Wind. Eng.* **2020**, *45*, 630–647. [CrossRef]

13. Savonius, S.J. Wind Rotor. U.S. Patent 1,766,765, 24 June 1930.

14. Abkar, M.; Dabiri, J.O. Self-similarity and flow characteristics of vertical-axis wind turbine wakes: An LES study. *J. Turbul.* **2017**, *18*, 373–389. [CrossRef]

15. Nguyen, V.D.; Jansson, J.; Goude, A.; Hoffman, J. Direct finite element simulation of the turbulent flow past a vertical axis wind turbine. *Renew. Energy* **2019**, *135*, 238–247. [CrossRef]

16. Sheidani, A.; Salavatidezfouli, S.; Stabile, G.; Rozza, G. Assessment of URANS and LES methods in predicting wake shed behind a vertical axis wind turbine. *J. Wind Eng. Ind. Aerodyn.* **2023**, *232*, 105285. [CrossRef]

17. Crooks, J.M.; Hewlin, R.L., Jr.; Williams, W.B. Computational Design Analysis of a Hydrokinetic Horizontal Parallel Stream Direct Drive Counter-Rotating Darrieus Turbine System: A Phase One Design Analysis Study. *Energies* **2022**, *15*, 8942. [CrossRef]

18. Karimian, S.M.H.; Abdolahifar, A. Performance investigation of a new Darrieus vertical axis wind turbine. *Energy* **2020**, *191*, 116551. [CrossRef]

19. Dadamoussa, A.; Boualem, K.; Yahiaoui, T.; Imine, O. Numerical investigation of flow on a Darrieus vertical axis wind turbine Blade with Vortex Generators. *Int. J. Fluid Mech. Res.* **2020**, *47*, 43–58. [CrossRef]

20. Al-Gburi, K.A.H.; Alnaimi, F.B.I.; Al-quraishi, B.A.; Tan, E.S.; Maseer, M.M. A comparative study review: The performance of Savonius-type rotors. *Mater. Today Proc.* **2022**, *57*, 343–349. [CrossRef]

21. Deda Altan, B.; Gultekin, G.S. Investigation of Performance Enhancements of Savonius Wind Turbines through Additional Designs. *Processes* **2023**, *11*, 1473. [CrossRef]

22. Shukla, V.; Kaviti, A.K. Performance evaluation of profile modifications on straight-bladed vertical axis wind turbine by energy and Spalart Allmaras models. *Energy* **2017**, *126*, 766–795. [CrossRef]

23. Anderson, J. *Computational Fluid Dynamics*; McGraw-Hill Education: New York, NY, USA, 1995.

24. Spalart, P.; Allmaras, P. A one-equation turbulence model for aerodynamic flow. *AIAA Pap.* **1992**, *12*, 439–478.

25. Rogers, S.; Kwak, D. Upwind differencing scheme for the time-accurate incompressible Navier-Stokes equations. *AIAA J.* **1990**, *28*, 253–262. [CrossRef]

26. Whitfield, D.L.; Taylor, L.K. *Numerical Solution of the Two-Dimensional Time-Dependent Incompressible Euler Equations*; NACA-CR-195775; Mississippi State University: Starkville, MS, USA, 1994; p. 65.

27. Fletcher, C.A.J. *Computational Techniques for Fluid Dynamics*; Springer Science & Business Media: Berlin/Heidelberg, Germany, 1991; p. 401.

28. Rogers, S.; Kwak, D. An upwind differencing scheme for the incompressible Navier-Strokes equations. *Appl. Numer. Math.* **1991**, *8*, 43–64. [CrossRef]

29. Prikhod'ko, A.; Redtchits, D. Numerical modeling of a viscous incompressible un-steady separated flow past a rotating cylinder. *Fluid Dyn.* **2009**, *6*, 823–829. [CrossRef]

30. Redchyts, D.; Gourjii, A.; Moiseienko, S.; Bilousova, T. Aerodynamics of the turbulent flow around a multi-element airfoil in cruse configuration and in takeoff and landing configuration. *East. Eur. J. Enterp. Technol.* **2019**, *9*, 36–41.

31. Redchyts, D.; Shkvar, E.; Moiseienko, S. Computational simulation of turbulent flow around truck-trailers. *Fluid Dyn. Mater. Process.* **2020**, *1*, 91–103.

32. Oler, J.W.; Strickland, J.H.; Im, B.J.; Graham, G.H. *Dynamic Stall Regulation of the Darrieus Turbine*; SAND 83–7029; Sandia National Laboratories: Albuquerque, NM, USA, 1983; p. 154.

33. Redchyts, D.; Moiseienko, S.; Shkvar, Y.; Shiju, E. Vortical systems, generated by Darrieus and Savonius Rotors. In Proceedings of the 9th International Conf. on Vortex Flow Mechanics, Rhodes, Greece, 20–25 June 2021; p. 37.

34. Redchyts, D. Numerical simulation of wind turbine rotors aerodynamics. *PAMM* **2008**, *7*, 2100049–2100050. [CrossRef]

35. Dzenzersky, V.; Tarasov, S.; Kostyukov, I. *Techeniya v Okrestnosti N-Rotora Dar'ye*; Nauk. Dumka: Kiev, Ukraine, 2013; p. 96.

36. Blackwell, B.; Sheldahl, R.; Feltz, L. *Wind Tunnel Performance Data for Two- and Three-Bucket Savonius Rotors*; SAND76-0131; Sandia National Laboratories: Albuquerque, NM, USA, 1976; p. 105.